Bubble Dynamics and Anode Effects in Aluminium Chloride Electrolysis: Experimental and Numerical Simulation

Cong Wang[1], Tianshuo Yang[2], Hongkun Niu[3], Zhiwei Liu[4], Sen Zhou[5], Mouhamadou Aziz Diop[6] and Bingliang Gao[7]
1, 3, 4, 5. Doctoral degree students
2. Master's degree student
6. Associate professor
7. Full professor
Northeastern University - School of Metallurgy, Shenyang, China
Corresponding author: blgao@mail.neu.edu.cn
https://doi.org/10.71659/icsoba2025-al054

Abstract

This study examines anode bubble dynamics and their role in the anode effect during aluminium chloride electrolysis (ACE) using a high-temperature transparent cell. Experiments were conducted in a NaCl-LiCl-$AlCl_3$ molten salt system at 750°C with graphite electrodes. Bubble behaviour was analysed under current densities ranging from 0.4 to 2.0 A/cm^2. Results show that bubble nucleation, growth, coalescence, and detachment follow a consistent pattern. Higher current densities accelerate bubble formation and reduce detachment intervals, while increasing bubble size and gas film thickness. The anode effect is characterized by a voltage surge to about 30 V and prolonged bubble release intervals (1.4–4.5 s). Before the anode effect, bubbles detach frequently (0.07–0.6 s), but during the anode effect, a stable gas film with a "big head, small tail" morphology is formed, disrupting the current flow. These findings highlight the critical link between bubble dynamics and cell stability, offering insights for optimizing ACE to minimize energy losses. The study advances understanding of ACE as a sustainable alternative to conventional aluminium production.

Keywords: Aluminium chloride electrolysis, Bubble dynamics, Anode effect, Transparent electrolytic cell, Current density.

1. Introduction

Aluminium chloride electrolysis (ACE), proposed as a promising technical alternative to the Hall-Héroult process [1–6], has received considerable attention since its announcement by Alcoa in 1973 [7]. Meanwhile, in 1976, Alcoa established a pilot plant with an annual capacity of 15 kt/y. The ACE process offers many advantages, including excellent energy efficiency across the entire production line. The electrolysis is conducted in a closed system, thereby minimizing pollution. It operates at a low temperature (around 700–800 °C), featuring a high current density (0.8–2.3 A/cm^2), and a very small cathode-anode distance can be maintained. Chlorine (Cl_2) is the only anode product, as shown in Equation (1), and can be recycled and used for the chlorination of bauxite or alumina to prepare aluminium chloride. Therefore, the carbon anode as a non-consumable anode does not generate greenhouse gases emissions [8]. Moreover, the anode-cathode distance (ACD) can be maintained lower than in the present Hall-Héroult cell, and a bipolar stacked electrode is used, which significantly improves the voltage utilization efficiency and demonstrates remarkable potential for energy conservation.

$$2AlCl_3\ (diss) \rightarrow 2Al\ (l) + 3Cl_2\ (g) \quad (1)$$

The bipolar electrolytic cell, due to the characteristics of the electrode arrangement, effectively prevents the molten aluminium from accumulating on the cathode surface. This feature not only

maintains a stable ACD but also eliminates the influence of metal movement caused by a strong magnetic field.

Hauksson and Foulkes [7] investigated voltage and current efficiency in a lab-scale electrolytic cell using graphite electrodes in the NaCl-LiCl-$AlCl_3$ molten salt at 700 °C. They systematically examined how $AlCl_3$ concentration, forced convection, electrode spacing, and current density affect current efficiency. Forced convection minimally impacted cathode polarization when $AlCl_3$ exceeded 2 wt.% but reduced diffusion control and concentration polarization at lower concentrations. Current efficiency increases sharply below 0.8 A/cm^2 but stabilizes at 80–90 % above this level. Factors such as forced convection, increased ACD, and rapid chlorine gas escape improve efficiency.

The behaviour of anode bubbles during the electrolysis process and the deposition characteristics of metallic aluminium on the graphite electrode are critical factors for ensuring stable operation of $AlCl_3$ electrolysis. Currently, there is a scarcity of studies focusing on the bubble dynamics during the aluminium chloride electrolysis process. Hence, in this study, the behaviour of anode bubbles was investigated using a transparent electrolysis cell and numerical simulations to elucidate the influence of current density on anode bubble dynamics and cell voltage.

2. Experimental and Mathematical Model

In this study, high-purity reagents were employed to ensure the reliability and reproducibility of the experimental results. The electrolyte used in the experiments was a mixture of NaCl (63.3 wt.%), LiCl (31.7 wt.%) and $AlCl_3$ (5 wt.%), which has a liquidus temperature of 650.2 ℃. Electrolysis temperature is maintained at 750 ℃. Sodium chloride (NaCl, 99 % purity), lithium chloride (LiCl, 99 % purity) and aluminium chloride ($AlCl_3$, 99 % purity) were fully dried to remove adsorbed moisture prior to use. The total mass of the electrolyte utilized in the electrolysis experiments was approximately 600 grams. The graphite anodes and cathodes were prepared using high-purity graphite (99 % purity) by Kejin Graphite Ltd, Shenyang, China.

A high-temperature transparent aluminium electrolysis cell (TAEC) [9], Figure 1 (a), was employed for studying the behaviour of anode bubbles in the melt. Figure 1 (b) shows the design of the side-observation transparent electrolysis cell, which consists of a two-chamber quartz crucible. The left chamber served as the anodic compartment with a dimension of 75 × 65 × 100 mm, while the right chamber functioned as the cathodic compartment with a dimension of 35 × 65 × 100 mm. The two chambers were connected by a 2-mm gap at the bottom of the middle wall, which allowed the current to flow from the anode compartment to the cathode compartment. The graphite anode had dimensions of 40 × 20 × 70 mm and featured an inclined angle of 5°. The anode was shielded by a boron nitride sleeve (as shown in Figure 1 (d)), resulting in a working anode surface area of 8.03 cm^2. The graphite cathode measured 30 × 15 × 70 mm (Figure 1 (c)). The electrolyte had a depth of 60 mm. Both the anode and the cathode were vertically immersed in the electrolyte, with depths of 40 and 30 mm, respectively.

The bubble behaviour was recorded at a speed of 60 frames per second (FPS) through a side window of the cell using a full-frame camera (Sony, Alpha7M2) equipped with a zoom lens (TAMRON, 70-300 mm F/4.5-6.3 Di III RXD). At another window of the electrolytic cell, a LED light source was utilized to capture higher-quality images. A DC power supply (IT6722A) was used to apply a constant DC current between the anode and the cathode. This power supply had a maximum power of 600 W and could simultaneously collect the cell voltage and the actual operating current. A K-type thermocouple was placed in the anode chamber to simultaneously monitor the temperature of the molten salt close to the anode, as shown in Figure 1 (b).

The experiments were conducted in the following sequence of anodic apparent current densities J_a: 0.8, 1.6, 1.0, 0.4, 1.7, and 2.0 A/cm^2. Each anodic current density (J_a) underwent three electrolysis experiments. After approximately 80 seconds of normal electrolysis, the power source was turned off and the cell voltage was stabilized before proceeding with the subsequent experiment. During the process, bubble morphology, cell voltage, and cell current were recorded simultaneously for the correlations between bubble behaviours and cell voltage drop.

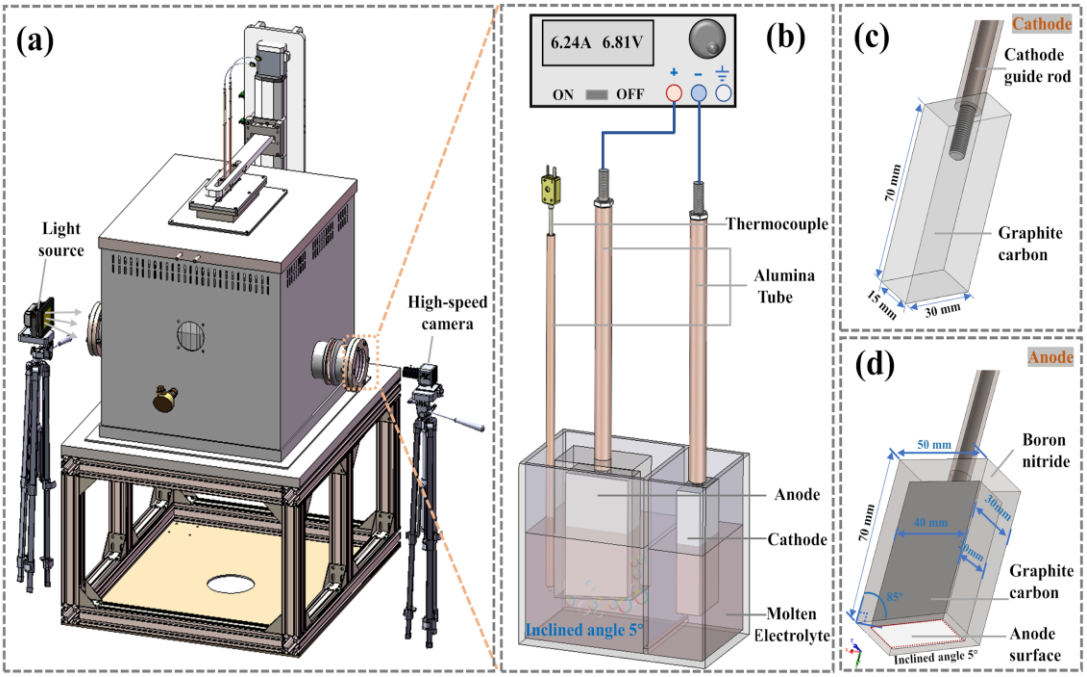

Figure 1. Experimental set-up, schematic diagram of the (a) high-temperature transparent aluminium electrolytic cell, (b) core electrolysis compartment with electrodes and DC power supply, (c) cathode, (d) anode.

3. Results and Discussion

3.1 Characteristics of Cell Voltage and Current under Different Current Densities

Figure 2 illustrates the relationships between cell voltage, current, current density, and electrolysis duration. Figure 2 (a) denotes the apparent current density, which is the ratio of the actual current to the anode surface area (8.03 cm^2). During the experiments, six different current densities were systematically applied to the anode: 0.4 A/cm^2, 0.8 A/cm^2, 1.0 A/cm^2, 1.6 A/cm^2, 1.7 A/cm^2, and 2.0 A/cm^2. When the current density was set at 0.4 A/cm^2, the cell voltage was 4.95 V, while the cell voltage reached 12.0 V when the current density was 2.0 A/cm^2. This relatively high cell voltage is primarily attributed to the unique characteristics of the crucible used in the experiment. The current is constrained to flow from the anode into the electrolyte through a narrow 2 mm gap at the bottom of the crucible.

A thorough analysis of Figure 2 reveals a significant correlation between cell voltage and current density. It is noteworthy that under applied current densities of 0.8 A/cm^2 and 1.6 A/cm^2 (the first electrolysis experiment in figure 2 (c)), the electrolysis process proceeded normally in each case, with both the cell voltage and operating current remaining relatively stable throughout. However, when the current density was set to 1.0 A/cm^2, 1.6 A/cm^2 (the second and third electrolysis experiments), or 1.7 A/cm^2, the cell voltage increased sharply to 30 V shortly after the onset of electrolysis (as detailed in Figure 2 (c)). Subsequently, the current transitioned from a stable to an unstable state, followed by a rapid decline, indicating the onset of an anode effect. The anode

effect is a common phenomenon in both cryolite-alumina-based aluminium electrolysis processes [9–11] and rare earth molten salt electrolysis [12–14].

When the apparent current density was 2.0 A/cm^2, the maximum detectable voltage was approximately 12 V, as illustrated in Figure 2 (c). This limitation arises due to the power constraint of the DC power supply, which necessitates a reduction in the maximum supply voltage to deliver a higher operating current. However, as shown in Figures 2(a) and 2(b), the operating current quickly dropped from 16.1 A and then fluctuated within a certain range after several seconds of electrolysis, indicating that an anode effect occurred. This behaviour was consistently observed in all three trials.

Initially, when the current density was set at 1.6 A/cm^2 (the first electrolysis), no anode effect was detected. However, electrodes that had previously undergone the anode effect twice, reducing the current density to 1.0 A/cm^2 resulted in the reappearance of the anode effect in all three experimental trials. This suggests that even at relatively low current densities, electrodes with prior exposure to the anode effect remain more susceptible to re-triggering the phenomenon. Furthermore, when the current density was decreased to 0.4 A/cm^2, the experiment proceeded normally without any occurrence of an anode effect, likely due to the fact that the current density had not reached the critical threshold value required for its initiation. During the occurrence of the anode effect, as it could not self-terminate, the power supply was manually turned off after a defined duration to kill the anode effect.

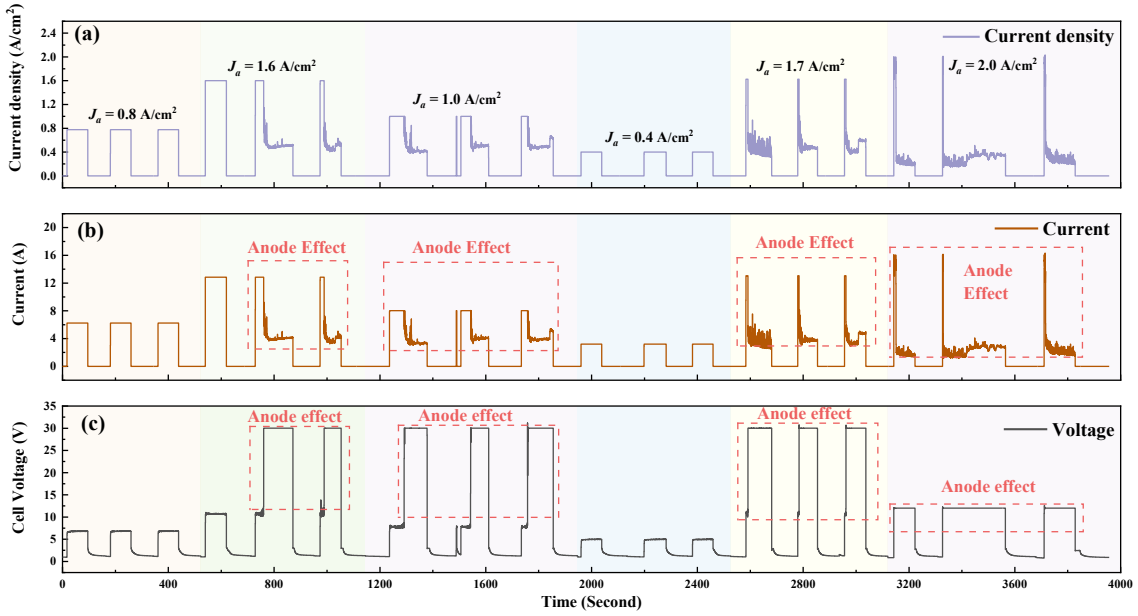

Figure 2. Variation of electrolysis parameters as a function of electrolysis time, (a) apparent current density, (b) current, and (c) cell voltage with graphite anodes at different anode current densities ranging from 0.4 to 2.0 A/cm^2.

3.2 The Bubble Behaviour and Characteristic Bubble Morphologies

In this study, the behaviour and morphology of bubbles at the anode bottom were systematically analysed under three current densities: 0.4, 0.8 and 1.6 A/cm^2.

Figure 3 illustrates the development and appearance of the bubbles on the shielded anode bottom. Upon the initiation of electrolysis, gas molecules are progressively generated. Simultaneously, larger bubbles are observed near the cathode-end region (Figure 3 (a-2), (b-2), and (c-2)), attributed to the higher local current density in this area. According to Faraday's law, the rate of

gas molecule generation is faster in regions with higher current densities. During the continuous growth of the bubbles, coalescence of smaller bubbles into larger ones was observed (as depicted in Figure 3 (a-2)-(a-3), (b-2)-(b-3), and (c-2)-(c-3)).

Following coalescence, the bubbles ascend along the anode surface under the combined influence of gravity, buoyancy, and surface tension, while continuously merging and growing with other bubbles during their upward motion. As shown in Figure 3, it is evident that the small bubbles exhibit quasi-spherical or ellipsoidal shapes.

When the growing bubbles are able to overcome the combined effects of gravity and surface tension (at t = 1.933 s, 0.867 s, and 0.55 s, respectively), they will detach from the side of the BN sidewall and exhibit behaviour analogous to that of large spherical bubbles, as illustrated in Figure 3 (a-5), (b-5), and (c-5). Following detachment, the large bubbles initially ascend along the side and subsequently begin further detachment at t = 2.017 s, 0.933 s, and 0.617 s, respectively. At this stage, the large bubbles adopt a "hat-like" morphology, as shown in Figure 3 (a-6), (b-6), and (c-6)). Subsequently, the bubble rises rapidly and reaches the surface of the electrolyte. It is worth noting that during the escape process of the large bubbles from the BN sidewall, the small bubbles at the anode bottom continue to follow similar patterns, including the gas formation, bubble nucleation, bubble growth, sliding, coalescence, and release.

In the experiments conducted at current densities of 0.4, 0.8 and 1.6 A/cm^2, a consistent mechanism for bubble nucleation and growth was observed. Specifically, at J_a = 0.4 A/cm^2 the first large bubble began to detach from the BN sidewall at t = 1.933 s (Figure 3 (a-5)), whereas for J_a = 0.8 and 1.6 A/cm^2 the detachment time decreased to 0.867 s and 0.55 s as depicted in Figure 3 (b-5) and (c-5). As the current density doubles, the time for the maximum bubble formation and detachment from the anode is halved approximately as well.

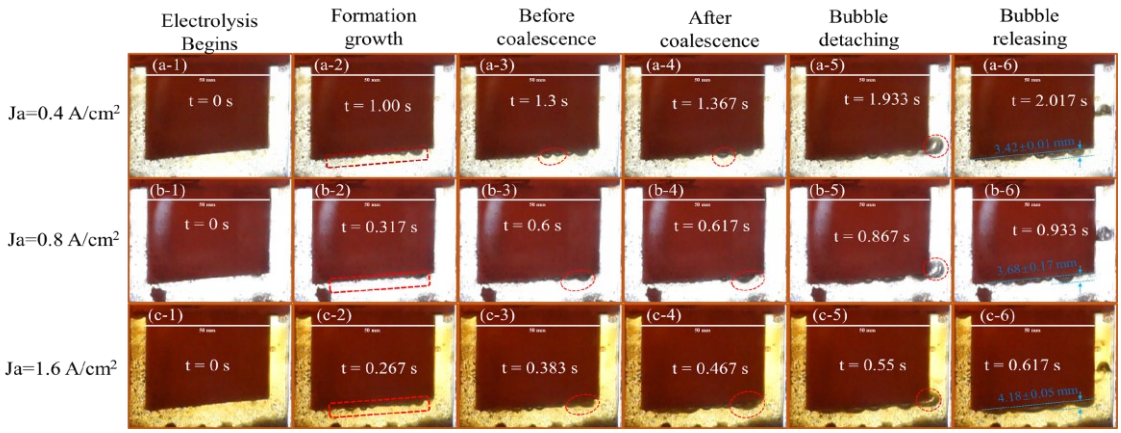

Figure 3. Anode bubbles behavior at the graphite anode bottom at different current densities of 0.4, 0.8, and 1.6 A/cm^2.

When the current densities J_a were set to 0.4, 0.8, and 1.6 A/cm^2, the maximum thicknesses of the bubble layer were measured as 3.42 mm, 3.68 mm, and 4.18 mm, respectively, as marked with blue dashed lines in Figure 3 (a-6), (b-6), and(c-6). It is evident that at J_a = 1.6 A/cm^2 the thickness of the bubble layer at the anode bottom was thicker compared to that of lower current densities. This can be attributed to the higher current density, which facilitated the rapid formation and growth of bubbles. Furthermore, some exceptionally large bubbles migrated to the front side, resulting in the release of certain bubbles from the sidewall in the frontal view at the current density of J_a = 1.6 A/cm^2.

3.3 The Anode Effect in Aluminium Chloride Electrolysis

The images in Figure 4 depict the anode effect process observed at the graphite carbon anode under test conditions. Figure 4 (1)-(14) illustrates the state immediately preceding the onset of the anode effect, with the anode operating at 1.6 A/cm^2 during the second electrolysis in Figure 2 (b).

As shown in Figure 4, according to the differences in the release frequency of large bubbles, the whole process can be briefly divided into three stages: the normal electrolysis stage, the transition stage, and the anode effect stage.

During normal electrolysis, the large bubble release intervals range from 0.07 seconds to 0.6 seconds. Especially, the bubble release interval is about 0.5 s prior to the anode effect, as shown in Figure 4 (1)-(6).

During the transition stage, the release frequency of large bubbles decreases significantly. The intervals between consecutive large bubble detachments range from 1.38 to 4.45 s (Figure 4 (8)-(14)). This phenomenon is closely associated with the abrupt decrease in current (Figure 2 (b)), which reduces the amount of gas generated.

Upon initiation of the anode effect, a continuous film of large gas bubbles forms at the anode bottom. The thickness of the bubble film reached 3.83 mm. These large bubbles consistently covered the anode bottom, exhibiting a distinctive morphology characterized by a larger head and smaller tail, and maintaining this morphological configuration until the power supply was turned off.

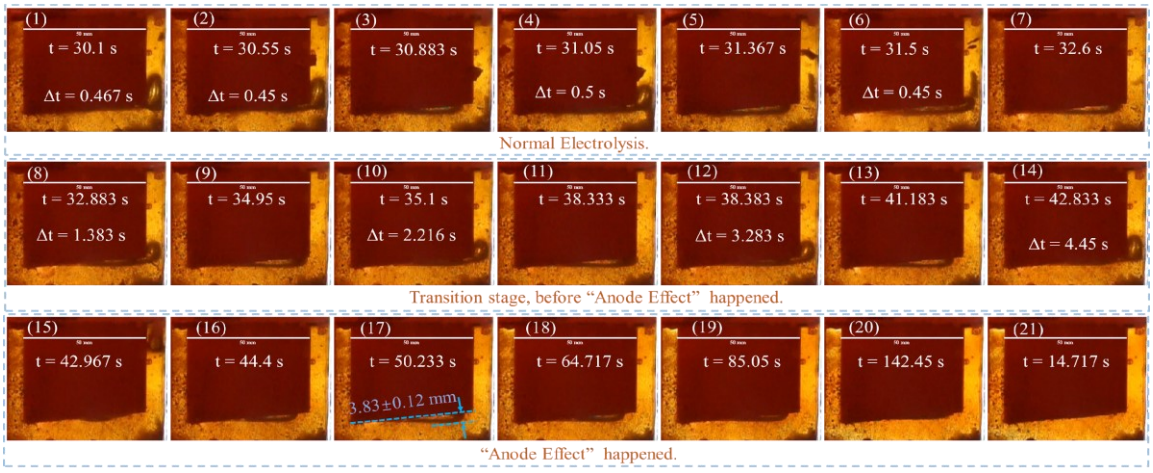

Figure 4. Anode bubbles profiles at the graphite anode working at an anode current density of 1.6 A/cm^2, where Δt represents the time difference between the large bubble and the preceding one.

In the Hall-Héroult electrolytic cells, it is widely recognized that an anode effect is triggered when the concentration of dissolved oxygen-containing ions becomes too low to sustain normal electrolysis. During the electrolysis of aluminium chloride, the anodic reaction involves the oxidation of chloride ions to produce gaseous chlorine, as illustrated in reaction (1) in Table 1. Notably, even under conditions of low aluminium chloride concentration, sufficient amounts of chloride ions or chloride-containing species are present in the molten electrolyte. Therefore, the occurrence of the anode effect cannot be attributed to a reduction of the chloride ion concentration, which contrasts with the mechanism observed in the conventional Hall-Héroult process.

Table 1 lists the main chemical reactions that may occur in the NaCl-LiCl-$AlCl_3$ molten salt system and their theoretical decomposition voltages. From the table, the theoretical decomposition voltage required to decompose $AlCl_3$ into gaseous chlorine (Cl_2) at 750 °C is 1.74 V, while the decomposition voltages required for the decomposition of NaCl and LiCl to generate Cl_2 are 1.54 V and 1.66 V higher than that of $AlCl_3$, respectively. In addition, as shown in Figure 2 (c), when the current density reached J_a = 1.6 A/cm^2, the cell voltage rose significantly from about 10.5 V during the anode effect. The abrupt rise in voltage is not attributable to a deficiency of aluminium ions at the cathode, which would otherwise lead to the reduction of sodium or lithium ions. Rather, it remains closely associated with alterations in the surface condition of the anode. A possible reason is that under high current density conditions, excessive amounts of chlorine gas bubbles are formed on the anode surface, resulting in a significant increase in the cell voltage and accompanied by the phenomenon of current "cut-off", that is, anode passivation. It was also found in the experiment that the anode effect cannot extinguish itself, which may be closely related to the generation kinetics of this type of "high-resistivity substance". The underlying mechanism of the anode effect still needs to be further explored in future research.

Table 1. Gibbs free energy of reaction and theoretical decomposition voltages for common reactions at 750 °C as solved by HSC chemistry 6.0

Reaction number	Chemical reaction equation	Gibbs free energy, ΔG (kJ/mol)	Electron transfer, n	Theoretical decomposition voltage, E^0 (V)
(1)	$2AlCl_3 = 2Al + 3Cl_2(g)$	1007.172	6	1.740
(2)	$2AlCl_3 + 1.5C = 2Al + 1.5CCl_4(g)$	1075.381	6	1.858
(3)	$2AlCl_3 + 2C = 2Al + C_2Cl_6(g)$	1150.838	6	1.988
(4)	$6NaCl = 6Na + 3Cl_2(g)$	1900.593	6	3.283
(5)	$6NaCl + 1.5C = 6Na + 1.5CCl_4(g)$	1968.802	6	3.401
(6)	$6LiCl = 6Li + 3Cl_2(g)$	1968.877	6	3.402
(7)	$6LiCl + 1.5C = 6Li + 1.5CCl_4(g)$	2037.086	6	3.519
(8)	$6NaCl + 2C = 6Na + C_2Cl_6(g)$	2044.259	6	3.531
(9)	$6LiCl + 2C = 6Li + C_2Cl_6(g)$	2112.542	6	3.649

As can be seen from Figure 2 (b) and (c), when the apparent current density reached J_a = 1.0 A/cm², an anode effect was observed. Figure 5 shows the simulation results of the current density at the anode bottom for J_a = 1.0 A/cm². In Figure 5, the current density range of the four edges at the anode bottom is 2.0–6.3 A/cm², significantly higher than the 0.39–0.8 A/cm² values in the central region of anode. The maximum current density appears at the two rightmost corners of the anode, reaching as high as 14.1 A/cm². In contrast, the current density of the anode at the far-cathode end is substantially lower than that near the close-cathode end regions. This phenomenon can be verified by the characteristics of the more bubbles and larger bubbles generated on the right side of the anode in Figure 3 (a-2), (b-2), and (c-2). In addition, Figure 5 shows that the average current density on the close-cathode end of the anode is approximately 4.0 A/cm². This value of current density can be referred to the critical current density for inducing the anode effect.

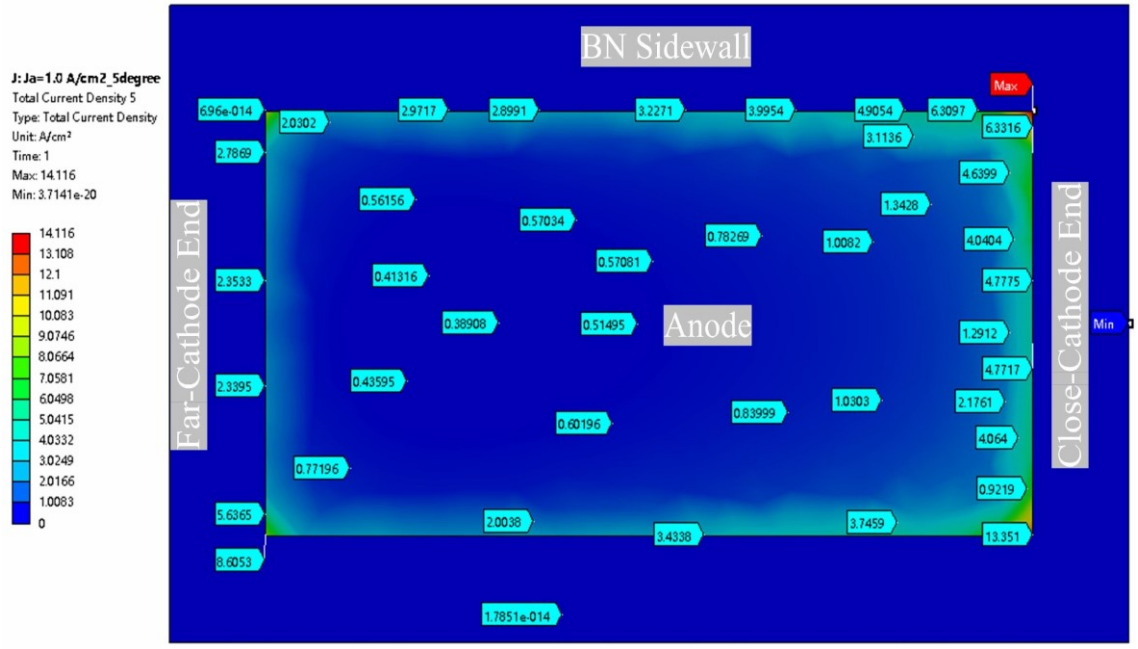

Figure 5. Simulated current density of the anode bottom surface, with an apparent current density J_a = 1.0 A/cm^2.

4. Conclusions

In this study, a high-temperature transparent electrolytic cell was utilized to directly observe bubble dynamics during the electrolysis process of $AlCl_3$ in NaCl-LiCl melts. Furthermore, the relationships between current density, bubble behaviour, and anode effects were systematically investigated. The main conclusions are as follows:

1) Under varying current density conditions, the behaviour of the bubbles at the anode bottom demonstrates consistency, including nucleation, growth, mutual coalescence, upward sliding along the inclined anode surface, further coalescence with other bubbles, and eventual detachment from the anode bottom.
2) The time interval between the detachment of large bubbles from the anode bottom is inversely proportional to the current density. Additionally, both the bubble size and the thickness of the gas film layer increase slightly with increasing anode current density.
3) During the anode effect, the cell voltage rapidly increases to approximately 30 V, accompanied by significant decline in the current. Prior to the onset of the anode effect, the release intervals for large bubbles range from 0.07 to 0.6 s; however, upon initiation of the anode effect, the intervals extend to 1.4 to 4.5 s. Numerical simulation shows the average current density at which the anode effect occurs is estimated to be approximately 4.0 A/cm^2.
4) Throughout the anode effect, large bubbles exhibit a distinctive morphological feature characterized by a "big head and small tail," which persist throughout the entire process.

5. References

1. Ling Ran et al., Fully-coupled electric-thermal-flow modeling and investigation of dynamic thermal-ledge behavior in aluminium electrolysis cell, *Journal of The Electrochemical Society*, 171, 2024, 093507. https://doi.org/10.1149/1945-7111/ad778f.
2. Warren E. Haupin, Principles of aluminium electrolysis, *Essential Readings in Light Metals* 2016, 3–11. https://doi.org/10.1007/978-3-319-48156-2_1.

3. Choon-Jie Wong et al., Studies on power modulation of aluminium smelting cells based on a discretized mass and thermal dynamic model, *Metallurgical and Materials Transactions B*, 54(2), 2023, 562–577. https://doi.org/10.1007/s11663-022-02709-w.
4. Guðrún Sævarsdóttir, Halvor Kvande and Barry J. Welch, Aluminium production in the times of climate change: the global challenge to reduce the carbon footprint and prevent carbon leakage, *JOM*, 72, 2020, 296–308. https://doi.org/10.1007/s11837-019-03918-6.
5. Bingliang Gao et al., Visualization of anode effect in aluminium electrolysis, *Journal of The Electrochemical Society*, 169(1), 2022, 013505. https://doi.org/10.1149/1945-7111/ac4bf5.
6. Niu Hongkun, Wang Cong, Gao Bingliang*, et al.,* A study of the passivating fluorocarbon (CF_x) film during electrochemical formation/co-evolution of CF_4 in aluminium electrolysis. *Ionics*, 30, 2024, 4811–4821. https://doi.org/10.1007/s11581-024-05635-w
7. Trausti Hauksson and Frank R. Foulkes, A study of the voltage and current efficiencies of fused salt $AlCl_3$ electrolysis using bench scale cells, *The Canadian Journal of Chemical Engineering*, 63(2), 1985, 237–243. https://doi.org/10.1002/cjce.5450630208.
8. Kai Grjotheim, A comment on the aluminium chlorine electrolyzing process for making aluminium, *Journal of Northeast Institute of Technology*, 1981, 27(2), 101–108.
9. Li Qingfeng and Qiu Zhuhan, Electrochemical Deposition of Aluminium from NaCl-$AlCl_3$ Molten Salt System. *Rare Metal Materials and Engineering*, 24(3), 1995, 59–63.
10. Hongkun Niu, Cong Wang, Bingliang Gao et al., Visualization of the impact of fluorocarbon (CF_x) passivation films and bubble layers on the anode effect, *Surfaces and Interfaces*, 2025, 59, 105968. https://doi.org/10.1016/j.surfin.2025.105968.
11. Gao Bingliang et al., Visualization of anode effect in high temperature transparent aluminium electrolysis cell, *Proceedings of the 41st International ICSOBA Conference,* Dubai, 5–9 November 2023, *TRAVAUX* 52, 1573–1580.
12. Hanno Vogel, Benedikt Flerus, Felix Stoffner and Bernd Friedrich, Reducing greenhouse gas emission from the neodymium oxide electrolysis. Part I: Analysis of the anodic gas formation, *Journal of Sustainable Metallurgy*, Vol. 3, 2017, 99–107. https://doi.org/10.1007/s40831-016-0086-0.
13. Hanno Vogel and Bernd Friedrich, Reducing greenhouse gas emission from the neodymium oxide electrolysis. Part II: Basics of a process control avoiding PFC emission, *International Journal of Nonferrous Metallurgy,* Vol. 6(3), 2017, 27–46. https://doi.org/10.4236/ijnm.2017.63003.
14. Lizhi Zhang, Xiufeng Wang and Bin Gong, Perfluorocarbon emissions from electrolytic reduction of rare earth metals in fluoride/oxide system, *Atmospheric Pollution Research*, 9(1), 2018, 61–65. https://doi.org/10.1016/j.apr.2017.06.006.